Internal structure of magnetic clouds: Plasma and composition

B. J. Lynch, T. H. Zurbuchen, and L. A. Fisk
Department of Atmospheric, Oceanic, and Space Sciences, University of Michigan, Ann Arbor, Michigan, USA

S. K. Antiochos
E. O. Hulburt Center for Space Research, Naval Research Laboratory, Washington, D. C., USA

Received 18 July 2002; revised 23 March 2003; accepted 26 March 2003; published 14 June 2003.

[1] A comprehensive analysis of magnetic clouds observed by the Advanced Composition Explorer (ACE) spacecraft from February 1998 to July 2001 is presented. The magnetic field data from the MAG instrument is fit with the cylindrically symmetric, linear force-free model and the fit parameter distributions are examined. This magnetic field model enables us to map plasma data from the SWEPAM and SWICS instruments to a position within the model cylinder. A superposed epoch analysis of all our magnetic cloud events is used to construct diameter cuts through an ''average'' cloud profile in any desired plasma, elemental composition, or charge state quantity. These diameter cuts are found to have nontrivial structure and there appears to be significant composition and structural differences between clouds of different speeds. The slow magnetic clouds ($\langle V_{rad} \rangle < 500$ km/s) have an almost constant proton density profile whereas the fast magnetic cloud ($\langle V_{rad} \rangle \geq 500$ km/s) profile is depleted throughout with symmetric dips and a local maximum at the cloud center. The fast magnetic clouds have a slightly higher N_α/N_p ratio than the slow clouds. Both the fast and slow events have enhanced oxygen and iron charge states compared to the slow solar wind. The fast events have a slightly increased O^{7+}/O^{6+} average profile and a much stronger $Fe^{\geq 16+}/Fe_{total}$ profile than the slow events. We briefly discuss the implications for physical conditions at the Sun, the role these coronal mass ejections (CMEs) may play in transporting magnetic flux, and the application of our structure results to the current flux rope CME modeling effort. *INDEX TERMS:* 2111 Interplanetary Physics: Ejecta, driver gases, and magnetic clouds; 7513 Solar Physics, Astrophysics, and Astronomy: Coronal mass ejections; 2164 Interplanetary Physics: Solar wind plasma; 2162 Interplanetary Physics: Solar cycle variations (7536); *KEYWORDS:* magnetic clouds, interplanetary coronal mass ejections (CME, ICME), solar wind ion charge states

Citation: Lynch, B. J., T. H. Zurbuchen, L. A. Fisk, and S. K. Antiochos, Internal structure of magnetic clouds: Plasma and composition, *J. Geophys. Res.*, *108*(A6), 1239, doi:10.1029/2002JA009591, 2003.

1. Introduction

[2] Magnetic clouds are the most well-ordered manifestation of coronal mass ejections observed in the interplanetary medium (ICMEs). Magnetic clouds are magnetically dominated ejecta with a relatively simple magnetic field geometry. This geometry defines a distinct signature which gives rise to the three criteria necessary for identification: (1) the magnetic field direction undergoes a smooth, monotonic rotation over a large angle, (2) the magnetic field strength is higher than average, and (3) the proton temperature is lower than average [*Burlaga*, 1991]. Anywhere from one-third [*Gosling*, 1990] to one-half [*Cane et al.*, 1997] of ICMEs exhibit some or all of these magnetic cloud characteristics. The duration of a typical magnetic cloud event at 1 AU can vary from several hours to days.

[3] The magnetic field structure of these clouds has been well studied and thus provides a convincing link between magnetic clouds and eruptive prominences at the Sun. The cloud's magnetic orientation is strongly correlated to those of filaments on the solar surface in both field direction and helicity [*Rust*, 1994, 1999; *Bothmer and Schwenn*, 1994, 1998]. Since filament polarity and helicity change with the solar cycle one would expect to see a similar change in magnetic cloud orientations assuming their origin was related to filaments. *Mulligan et al.* [1998] have shown this clear solar cycle variation in magnetic cloud orientation strengthening the link between the two phenomena.

[4] In addition to the magnetic signatures of ICMEs, elemental composition and charge state measurements have become an important tool in describing the solar environment of the ICME origin [e.g., *Geiss et al.*, 1995]. Solar wind charge state measurements have become routinely available with the composition measurements from the Solar Wind Ion Composition Spectrometer (SWICS) that has been part of the ACE and Ulysses investigations [*Gloeckler et al.*, 1998, 1992]. ICMEs are often associated with unusual charge state compositions, indicating a thermal environment during the CME initiation that is very different

0148-0227/03/2002JA009591

from the physical conditions characterizing the average solar wind [*Galvin*, 1997 and references therein]. This might be expected based on remote sensing measurements of coronal ejecta.

[5] With recent LASCO observations, CME events are routinely associated with disappearing filaments/erupting prominence material [*Dere et al.*, 1999; *Plunkett et al.*, 2000]. This could result in a prediction for low charge state ions within ICMEs. Such time periods have been observed based on the measurements of He^{+} that is not usually present in the solar wind [*Schwenn et al.*, 1980; *Zwickl et al.*, 1983]. More recently, *Burlaga et al.* [1998] have seen a small region of very cold, dense material with unusual ion charge states consistent with expected prominence temperatures in a CME in January 1997. *Skoug et al.* [1999] saw a prolonged enhancement of He^{+} over the latter half of a magnetic cloud in ACE data in May 1998, and *Gloeckler et al.* [1999] observed a wide variety of both unusually low and unusually high ion charge states during the same event.

[6] Such observations are indicative of plasma related to prominence material. However, these "cool" events are very rare. During the entire time period during which reliable composition data are available by WIND and ACE, fewer than 10 events were observed with unusually low charge state ratios. Instead, most CMEs are associated with unusually high charge states, indicating a heated electron environment during the initiation and eruption. While a heated electron environment is most likely the cause, high ion charge states may also be caused by superthermal electrons [e.g., *Owocki and Scudder*, 1983; *Esser and Edgar*, 2000] or hot, high density ions [e.g., *Bürgi and Geiss*, 1986].

[7] The heavy ion charge state ratios are ratios of the measured ion densities. High oxygen charge states were studied by *Henke et al.* [1998, 2001] and *Reinard et al.* [2001], showing many CMEs are associated with O^{7+}/O^{6+} >1.0. *Lepri et al.* [2001] has confirmed previous indications that high iron charge states $Fe^{\geq 16+}$ are a good identifier of CME material [e.g., *Bame et al.*, 1979; *Fenimore*, 1980; *Galvin*, 1997].

[8] This paper presents a supplement to the traditional analysis of magnetic clouds by emphasizing the internal structure of the plasma and charge states derived from the inherent geometry of the linear force-free magnetic field model. Section 2 describes the ACE data and our event selection procedure. The linear force-free model and parameter fitting are reviewed in section 3, and our fitting results are presented in a larger solar wind/solar cycle context in section 4. In section 5 we describe our method of inferring spatial position and the results of the superposed epoch analysis: significant internal structure and its differences between fast and slow events. Section 6 includes a brief discussion of the implications of the composition differences between clouds of different velocities but otherwise identical magnetic signatures as well as some possible constraints this structure has on various magnetic cloud or flux rope CME creation models.

2. Data Description and Event Selection

[9] We have identified and modeled 56 magnetic cloud events observed by the ACE spacecraft between February 1998 and July 2001. The magnetic field data were from the Magnetic Field Experiment (MAG) instrument [*Smith et al.*, 1998], the plasma data were from the Solar Wind Electron Proton Alpha Monitor (SWEPAM) instrument [*McComas et al.*, 1998], and the ion charge states were from the Solar Wind Ion Composition Spectrometer (SWICS) instrument [*Gloeckler et al.*, 1998]. One hour data averages were used for all quantities throughout this study with the exception of the high iron charge states, which were 2 hour averages to enhance statistics.

[10] Figure 1 shows a magnetic cloud event from 25 September 1998 (DOY 268). The first three panels are the magnetic field magnitude, latitude δ, and longitude λ in RTN coordinates. The enhanced field magnitude and smooth rotation are evident in this particularly good example. The fourth panel is the radial velocity which shows a steady decrease throughout the event, consistent with cloud expansion. The fifth and sixth panels are proton density N_p and temperature T_p. The proton temperature has well defined boundaries and is clearly "low" during the event compared to the surrounding solar wind. Here, Figure 1 is again an excellent example, and the proton temperature signature is usually less ordered. The remaining panels are the composition measurements we will focus on: the density ratio of alpha particles to protons N_α/N_p, and the high oxygen and iron charge state ratios, O^{7+}/O^{6+} and $Fe^{\geq 16+}/Fe_{total}$. All three of these quantities indicate ICME material. The *Borrini et al.* [1982] enhanced helium ICME identification criteria, $N_\alpha/N_p > 0.08-0.10$, is met during most of the cloud. The O^{7+}/O^{6+} ratio >1.0 is higher than the upper limit of the slow solar wind distribution [*Zurbuchen et al.*, 2002; *von Steiger et al.*, 2000], and *Lepri et al.* [2001] showed convincingly that $Fe^{\geq 16+}/Fe_{total} > 0.1$ virtually always overlaps with other ICME indicators. Some of these enhancements even extend beyond the magnetic field defined boundaries. This event was also relatively fast, $\langle V_{rad} \rangle \sim 600$ km/s. We will show these types of composition enhancements are more common in clouds of this velocity class.

[11] Our magnetic cloud events are initially selected through visual inspection of 27-day plots of the magnetic field and proton temperature time series, using the *Burlaga* [1991] criteria as a starting point. The smooth field rotation was required for all events. The linear, force-free cylinder described in section 3 can model up to a 180° total field rotation but has difficulty with small field rotations less than $\sim 30-50°$ between the two spherical coordinate angles. Some authors include the "no rotation" limit as a qualifying smooth rotation (D. Berdichevsky, private communication, 2002), but in this study we have not.

[12] The enhanced field and low proton temperature were qualitatively compared with the ambient solar wind values on this 27-day timescale. The reference field enhancement tended to be >50% with some exceptions. For events with well defined low proton temperature boundaries (such as in Figure 1), the field enhancement requirement was sometimes relaxed to allow approximate equality with the surrounding solar wind. These cases have been described as "old" magnetic clouds (C. Smith, private communication, 2002) whose internal field strength has evolved to match the surrounding solar wind value but retain the magnetic shape and plasma characteristics of a magnetic cloud. These

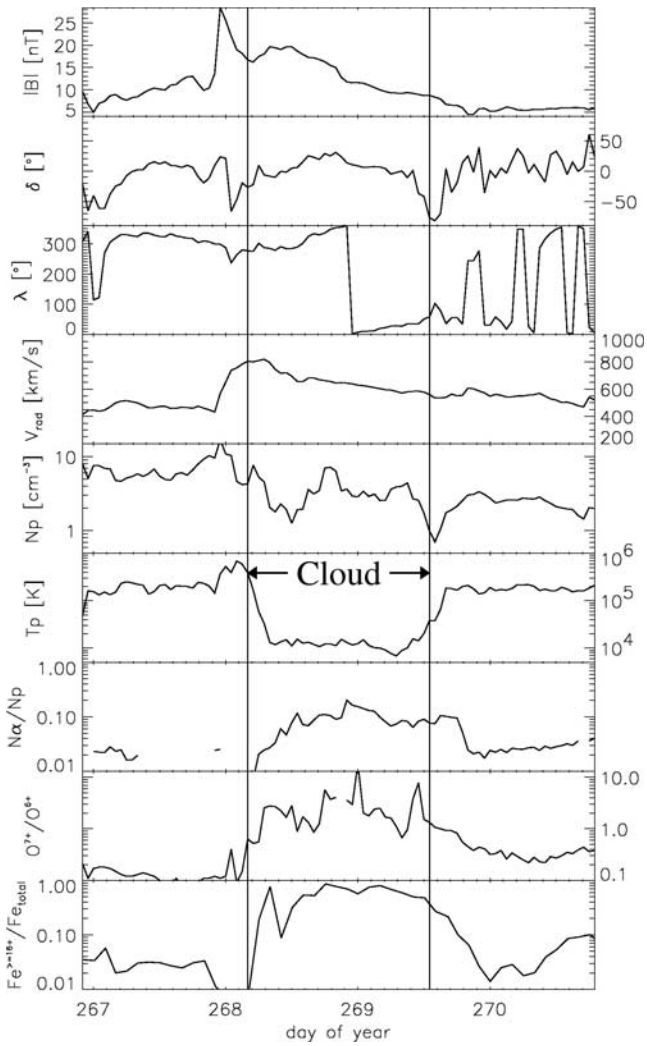

Figure 1. ACE data from the 25 September 1998 magnetic cloud event plotted against day of year. The cloud boundary is indicated by the vertical solid lines (see text for details). Here δ and λ are the magnetic field latitude and longitude in RTN coordinates. There is a N_α/N_p data gap before the cloud. All data are 1-hour averages except the high iron charge state ratio, which are 2-hour averages.

events have been included because of our interest in the internal plasma structure which related more to the magnetic geometry. The level of magnetic field enhancement can be inferred from the model fit parameter B_0 discussed in section 3.2. The proton temperature values tended to be significantly lower than the immediately surrounding solar wind, often with well defined boundaries. There were a number of events where the proton temperature boundaries were not well defined but the values were still low compared with the solar wind on a Carrington rotation timescale. This was a crude, qualitative approximation to the more velocity dependent quantitative measure of low proton temperature used by *Richardson and Cane* [1995] for ICME identification.

[13] Once a candidate event was identified, the exact boundaries were selected. There is still not a robust, quantitative boundary identification procedure (L. Burlaga, private communication, 2002), thus our boundary selection was a qualitative and somewhat iterative process. After our first guess based on the maximum extent of the field rotation, we checked for sharp changes in **B**, T_p, or V_{rad} within a couple of hours of the initial boundaries. If so, we used that change as the new boundary. This tended to yield a fairly conservative estimate of the cloud region and it was not uncommon for one or more of the classic characteristics to extend beyond our selected region.

[14] The fuzziness of the boundary selection is by no means detrimental to our final results. Since most events are ~10–30 hours in duration, ±1 hour is at most 10% of the cloud. The limitations of the model and the systematic uncertainties in fitting (discussed in section 3.3) have at least the same order error.

[15] For completeness, we would like to note that *Shimazu and Marubashi* [2000] have used the third derivative of the field components as a quantitative measure of smooth rotation to identify flux ropes. Using this measure, the boundary selection comes naturally as the first/last points to fit the selection criteria. However, this method also selects regions which cannot be fit with the linear force-free cylinder, so in this study we have employed the more traditional identification techniques described above.

3. Model Description and Fitting Technique

3.1. Linear Force-Free Cylinder

[16] *Goldstein* [1983] proposed that large interplanetary magnetic field rotations could be described as a cylindrical force-free flux rope. *Burlaga* [1988] introduced what has become the standard model for the internal magnetic field configuration within these clouds: cylindrically symmetric, force-free, with constant α, where α is the magnitude of the magnetic helicity. In general, α is a function of radial distance and an entire class of solutions could be considered from an appropriate generating function [*Lust and Schluter*, 1954]. The force-free configuration is a minimum energy state for a given helicity. Intuitively, one suspects that regardless of the original configuration, the magnetic fields in these clouds are likely to relax toward a force-free state. In order for this force-free state to be linear, i.e., constant α, a tremendous amount of internal reconnection must have taken place. While this may be the case in magnetic cloud ICMEs, it is by no means certain.

[17] The constant α configuration is the *Lundquist* [1950] solution of the equation for force-free magnetic fields,

$$\nabla \times \mathbf{B} = \alpha \mathbf{B}. \tag{1}$$

In cylindrical coordinates, this yields field components,

$$B_\rho = 0, \quad B_\phi = HB_0 J_1(\alpha\rho), \quad B_z = B_0 J_0(\alpha\rho). \tag{2}$$

Here B_0 is the field magnitude on the cylinder axis, ρ is the distance from the axis, H is the sign of the helicity, and J_0, J_1 are zeroth and first order Bessel functions. The constant value of α is determined by the radius of the cloud model cylinder R_c such that their product is the first zero of J_0.

[18] The cylinder orientation in space is described by three parameters. The axis orientation with respect to the ecliptic is given by two angles, ϕ_0, θ_0, while the distance

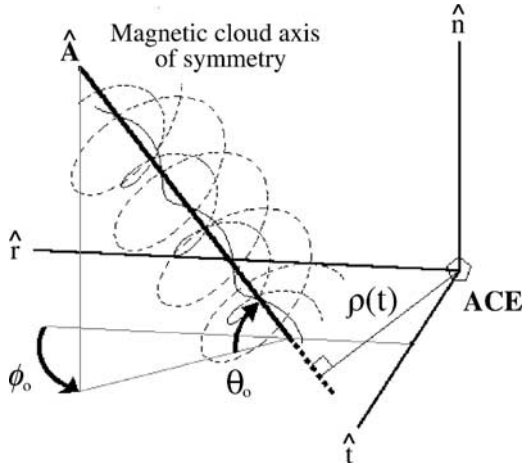

Figure 2. Geometry of the magnetic cloud cylinder model as it passes by the spacecraft. Several helical magnetic field lines given by equation (2) are shown as solid and dashed lines. The two angles ϕ_0, θ_0 define the cylinder axis orientation with respect to the ecliptic and $\rho(t)$ is the distance to the spacecraft perpendicular to the cloud axis. The impact parameter ρ_0 is the distance of closest approach.

between the spacecraft and the cylinder axis at the normalized closest point of approach is ρ_0. A cloud event for which the spacecraft trajectory goes right through the symmetry axis would have $\rho_0 = 0$, while the outer cloud boundary is defined as $\rho_0 = 1$. The direction of ρ_0 is taken to be the y-axis in the cloud frame. Figure 2 shows these parameters in a schematic for the cloud axis moving past the spacecraft in ACE-centered coordinates (RTN).

3.2. Fitting Procedure

[19] We have adopted the two-step least-squares fitting routine for parameter optimization described by *Lepping et al.* [1990] and will briefly review it here. The first step of the fitting procedure is to fit the cylinder direction and impact parameter. This is done by minimizing χ^2_{dir}, defined as the sum of the mean square error between the unit normalized data and model (B^M) field components. The second fit is solely for the axial field strength B_0 and is obtained by minimizing χ^2_{mag}, the mean square error between the data and model field magnitudes.

$$\chi^2_{dir} = \frac{1}{N}\sum_{i=1}^{N}\left(B_x - B_x^M\right)^2 + \left(B_y - B_y^M\right)^2 + \left(B_z - B_z^M\right)^2 \qquad (3)$$

$$\chi^2_{mag} = \frac{1}{N}\sum_{i=1}^{N}\left(|\mathbf{B}| - |\mathbf{B}^M|\right)^2 \qquad (4)$$

Here, N is the number of data points during the event.

[20] Table 1 lists each set of model fit parameters and their corresponding direction and magnitude errors. The linear force-free cylinder does a much better job modeling the field rotations than the field magnitude. This is represented in the χ^2_{dir} and χ^2_{mag} errors. The χ^2_{dir} error is used to evaluate the quality of the model fit. A good fit typically has $\chi^2_{dir} < 0.13$, a moderate fit is approximately 0.13–0.20, and $\chi^2_{dir} > 0.20$ is generally a poor angle fit.

[21] The χ^2_{mag} errors cannot be classified in a similar manner because of the varying "background" field strength. To illustrate this, Figure 3 shows a couple different model fits. The dotted lines are the data and the thick solid lines are the model. The left event is a moderate angle fit with a typical magnitude error, and the right event is a good angle fit with a relatively large magnitude error.

3.3. Best-Fit Parameter Distributions

[22] Figure 4 shows our model parameter distributions for the spatial orientation parameters, ϕ_0, θ_0, ρ_0, the axial magnetic field strength B_0, the cloud radius R_c, and the event averaged radial velocity $\langle V_{rad}\rangle$. In each plot the outlined bars are the slow cloud distribution and the thick-lined gray bars are the fast cloud distribution. This is evident from the $\langle V_{rad}\rangle$ histogram where we have classified slow cloud events as having $\langle V_{rad}\rangle < 500$ km/s and fast clouds $\geq$500 km/s.

[23] The two speed categories were created after it had become apparent that the faster events had stronger enhancements in the heavy ion charge states. The dividing line of 500 km/s was chosen because of a slight indication of a local minimum in the average velocity distribution, although this is not visible on the scale of the $\langle V_{rad}\rangle$ histogram of Figure 4. There were 44 slow cloud events and 12 fast cloud events. More events are needed in the ~500 km/s range to determine if the composition results of section 5 are truly bimodal or just the two ends of a continuous transition.

[24] Table 2 summarizes the averages and standard deviations for the distributions of Figure 4. In general, our parameter distributions agree with the results of other surveys. *Lepping et al.* [1990] found parameter averages very similar to ours: $\langle\phi_0\rangle = 106 \pm 38°$, $\langle\theta_0\rangle = -15 \pm 47°$, $\langle\rho_0\rangle = 0.22 \pm 0.22$, and $\langle B_0\rangle = 19.6 \pm 6.5$ nT. *Bothmer and Schwenn* [1998] assumed $\rho_0 = 0$ as found average axis orientation angles of $\langle\phi_0\rangle = 91 \pm 44°$, and $\langle\theta_0\rangle = 3 \pm 35°$.

[25] The ϕ_0 distributions for fast and slow clouds are similar, while the θ_0 distributions have averages that differ by approximately 15°. The fewer number of fast cloud events and the large rms prohibits drawing any solid conclusions about the polar angle distribution. The impact parameter distributions are similar for the two velocity classes. The fitting procedure appears to have a bias toward a zero or almost zero impact parameter, as evident in both fast and slow distributions. *Russell and Mulligan* [2002] have argued that the impact parameter distribution can be easily explained with an ellipsoidal flux rope geometry. The cylindrical model used here would systematically underestimate the impact parameter if this were the case.

[26] The fast clouds appear to have stronger on-axis magnetic fields but show more statistical variation. One supposes if the cloud's radial velocity was related to the creation mechanism, fast clouds would have more energy and thus stronger magnetic fields. One must be a little cautious however, as the 1 AU velocity is a combination of the original CME velocity and the interaction of the ejecta with the background solar wind during transit. The fast cloud radii are only slightly larger on average than their slower counterparts, although the shape of the R_c distributions is again almost the same. In general, the fast and slow

Table 1. ACE Magnetic Cloud Events and Model Fit Parameters

Year	DOY	Time, UT	Δt, hr	ϕ_0, deg.	θ_0, deg.	ρ_0, R_c^{-1}	H	B_0, nT	R_c, AU	$\langle V_{rad} \rangle$, km/s	Mag. Dir.[c]	Hand	χ^2_{dir}	χ^2_{mag}
1998	35[a,b]	0200	38	175.5	−0.4	0.0	−1	13.8	0.011	311.2	SWN	RH	0.091	0.25
	63	1400	37	296.4	17.9	0.0	1	13.2	0.133	341.7	SEN	LH	0.051	1.14
	65[b]	2000	17	40.4	−26.1	0.0	1	7.1	0.045	319.2	SWN	RH	0.180	0.52
	122[a]	1200	27	166.4	−20.9	0.0	1	11.9	0.072	550.0	ESW	RH	0.165	8.54
	165[b]	1000	18	10.6	30.0	0.0	1	11.3	0.037	345.3	WNE?	RH	0.128	3.65
	175	1300	27	314.9	19.4	0.0	1	14.5	0.108	464.5	SEN	LH	0.066	2.61
	209[a]	1600	15	81.4	−57.7	0.0	1	7.6	0.054	323.7	ESW	RH	0.241	7.56
	220	0700	30	278.5	33.6	0.50	1	8.4	0.169	423.4	ENW	LH	0.269	0.61
	214	0700	22	316.3	43.1	0.0	1	5.9	0.084	393.6	ENW	LH	0.260	1.73
	232[a]	0700	36	108.8	2.1	0.0	1	16.2	0.131	330.0	SWN	RH	0.161	4.13
	268	0400	34	0.0	49.5	0.45	−1	19.5	0.223	660.4	ENW	LH	0.146	18.98
	292	0400	27	252.4	−19.5	0.0	1	20.1	0.117	392.5	SEN	LH	0.148	32.61
	313	0200	24	225.0	−89.0	0.20	−1	17.9	0.125	444.9	ESW	RH	0.100	13.68
	326[a,b]	2000	15	336.9	−31.7	0.0	−1	7.8	0.036	341.8	ESW	RH	0.245	1.45
	345[b]	0400	12	345.3	−69.7	0.0	−1	15.3	0.044	354.3	ESW	RH	0.101	3.88
1999	4[a]	0900	28	298.8	−64.4	0.08	−1	9.6	0.105	330.0	ESW	RH	0.117	1.63
	49	1400	23	154.3	−31.3	0.0	−1	11.5	0.100	593.8	ESW	RH	0.333	11.07
	50	2100	22	304.0	22.6	0.0	−1	6.7	0.096	445.5	NES	RH	0.215	1.47
	106	2000	23	319.9	−35.2	0.06	1	22.8	0.085	411.5	WSE	LH	0.087	1.52
	111	0900	29	278.5	−18.1	0.02	1	9.3	0.160	480.6	SEN	LH	0.162	2.97
	173[a]	0600	17	328.1	55.6	0.03	1	6.8	0.060	350.0	ENW	LH	0.233	1.04
	189[a]	0200	17	95.2	−27.8	0.0	−1	10.4	0.075	392.2	NWS	LH	0.086	0.97
	221	1100	28	226.0	65.3	0.55	1	14.1	0.126	339.8	ENW	LH	0.102	3.98
	234	0800	22	293.6	−63.7	0.01	1	8.9	0.102	410.8	ESW	RH	0.111	3.36
	294	0400	16	130.6	−13.7	0.40	−1	25.4	0.068	449.7	NWS	LH	0.195	23.28
	361	1600	14	169.8	−17.2	0.08	−1	9.7	0.023	440.0	WSE?	LH	0.245	0.70
2000	52	1300	23	0.0	63.1	0.0	1	18.2	0.089	378.5	WNE	RH	0.158	7.29
	69	2000	13	180.0	60.7	0.17	1	6.8	0.049	384.4	ENW	LH	0.592	0.95
	91	0800	26	46.8	−0.6	0.10	1	8.6	0.082	374.4	SWN	RH	0.138	2.09
	110	0400	11	315.9	−6.3	0.46	−1	13.2	0.042	448.3	NES	RH	0.115	2.03
	128[b]	0000	18	179.8	52.3	0.26	1	9.2	0.067	401.7	WNE	RH	0.161	2.35
	193	2300	27	329.8	30.9	0.01	1	12.0	0.105	503.5	ENW	LH	0.156	2.29
	197	1900	18	244.3	28.9	0.0	1	44.3	0.160	849.1	SEN	LH	0.128	155.3
	209	0800	21	135.5	−21.1	0.0	−1	7.5	0.062	346.5	NWS	LH	0.245	2.44
	210	2200	15	129.8	−38.5	0.0	−1	14.5	0.067	463.0	WSE	LH	0.252	7.76
	213	2200	18	323.6	−9.1	0.0	−1	13.3	0.056	454.3	NES	RH	0.186	4.17
	223	1800	22	287.6	−47.8	0.02	1	14.4	0.105	425.2	WSE?	LH	0.225	4.41
	225	0500	25	280.4	20.8	0.0	1	28.5	0.164	576.7	SEN	LH	0.126	45.60
	246	2200	16	0.0	37.5	0.02	1	8.8	0.046	419.2	WNE	RH	0.255	6.11
	262	0100	25	128.0	5.0	0.31	−1	21.2	0.174	727.5	NWS	LH	0.306	70.58
	277	1500	36	242.8	14.2	0.29	−1	17.9	0.157	399.3	NES	RH	0.236	11.91
	287	1700	23	300.4	−33.2	0.0	−1	14.5	0.096	400.0	NES	RH	0.118	7.37
	302	2100	27	283.5	−16.2	0.01	1	16.3	0.116	380.1	SEN	LH	0.148	16.84
	311	2200	19	280.0	11.3	0.03	1	24.1	0.114	534.4	SEN	LH	0.049	13.68
	333	2300	19	233.6	−68.5	0.0	1	12.1	0.109	520.1	WSE	LH	0.308	1.85
	364	1900	13	265.3	32.8	0.56	1	11.8	0.063	361.5	SEN	LH	0.139	1.65
2001	78[a,b]	1900	46	319.0	−63.5	0.01	1	19.2	0.183	360.0	WSE	LH	0.108	4.38
	86	2000	10	281.6	18.3	0.43	1	17.4	0.071	606.5	SEN	LH	0.110	17.65
	102	0400	15	103.0	49.0	0.0	1	17.8	0.106	640.6	WNE	RH	0.136	20.37
	112	0000	27	141.1	−47.2	0.45	−1	14.9	0.105	355.2	WSE	LH	0.074	5.09
	119	0000	14	322.5	1.2	0.01	1	11.1	0.059	624.3	SEN	LH	0.033	1.29
	127	1800	15	170.0	0.0	0.70	−1	12.3	0.015	361.6	NWS	LH	0.386	0.41
	129	1200	32	138.0	−28.4	0.0	1	9.1	0.121	430.5	SWN	RH	0.132	3.49
	148	1100	23	218.3	−19.1	0.38	1	12.2	0.086	451.6	SEN	LH	0.094	1.22
	190	0200	14	96.7	57.5	0.63	1	6.3	0.089	437.5	SWN	RH	0.114	3.29
	191[a]	1000	24	49.9	−15.7	0.36	1	8.6	0.093	369.2	SWN	RH	0.211	1.47

[a]Event has a data gap in some or all SWEPAM measurements (N_p, T_p, V_{rad}, N_α/N_p).
[b]Event has a data gap in some or all SWICS measurements (O^{7+}/O^{6+}, $Fe^{\geq 16+}/Fe_{total}$).
[c]Question mark indicates some ambiguity in the classification of projected Y-Z field rotation; see section 4.2 text for details.

clouds appear to be fairly similar in their model fit parameters and the statistical uncertainties in the B_0 and R_c distributions prohibit any significant conclusions being drawn about their relation to cloud speed.

3.4. Limitations and Fit Parameter Uncertainties

[27] The linear force-free cylinder model is a simple but very useful analysis tool. It is important to understand the limitations of this model. We have briefly mentioned the discrepancy between the field direction and magnitude fit errors, due mostly to the model's inherent symmetry and the ~2:1 center-to-edge field strength. We have found that the model fit parameters are not independent near the error minimums of equations (3) and (4). We will also present a rough estimate for the systematic uncertainty in the best fit parameter ρ_0 and compare it to the more sophisticated estimate by *Lepping et al.* [2002].

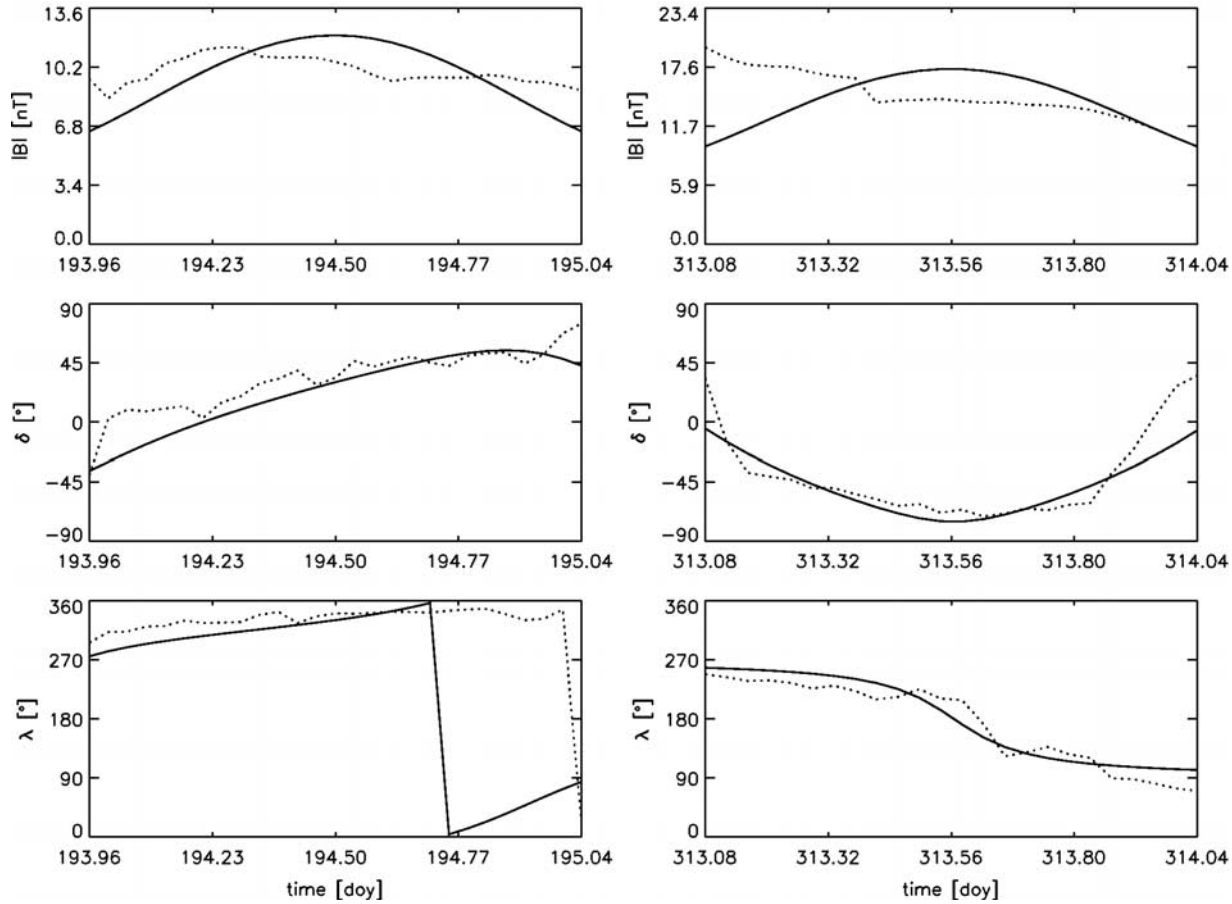

Figure 3. Two magnetic cloud model fits plotted versus time (day of year). The dotted lines are the ACE MAG data, the field magnitude, latitude (δ), and longitude (λ) in RTN coordinates. The solid lines are the model fits described in section 3. (left) The 12 July 2000 (DOY 193) event shows a moderate angle fit $\chi^2_{dir} = 0.156$ and a typical magnitude error $\chi^2_{mag} = 2.29$. (right) The 9 November 1998 (DOY 313) event shows a good angle fit $\chi^2_{dir} = 0.100$ and one of the higher magnitude errors, $\chi^2_{mag} = 13.68$.

[28] The routine used to implement the least squares fitting also calculates the covariance between parameters during optimization. The first fit adjusts ϕ_0, θ_0, and ρ_0. Since H only has two values, ±1, it is too constrained for our minimization routine to vary. The average correlation coefficients between the spatial variables were $cc_{\phi\theta} = 0.06 \pm 0.56$, $cc_{\phi\rho} = -0.24 \pm 0.82$, and $cc_{\theta\rho} = 0.01 \pm 0.73$. The high rms error indicates that despite low average correlations over our entire set of events, in each individual fit the parameters were often highly correlated. The average absolute values of these coefficients were $|cc_{\phi\theta}| = 0.45 \pm 0.34$, $|cc_{\phi\rho}| = 0.79 \pm 0.31$, and $|cc_{\theta\rho}| = 0.63 \pm 0.35$.

[29] Since the axial magnetic field magnitude B_0 is fit singularly holding the rest of the parameters fixed, its correlation coefficients are generated separately after the initial fitting. There was no correlation between B_0 and ϕ_0 or θ_0. We would expect some correlation between B_0 and the impact parameter ρ_0 because of the functional dependence. We found there was less variation in this lower correlation, $cc_{B\rho} = 0.15 \pm 0.15$.

[30] All of the spatial structure of section 5 is inferred from the geometry of the static, linear force-free magnetic field model. The systematic model uncertainty inherent in the best fit parameter ρ_0 propagates through our mapping procedure. In order to examine this effect on the results of section 5 we need to quantify this systematic uncertainty.

[31] If we treat the observed magnetic field component B_i as a Gaussian random variable distributed about the model value B_i^M with a unit variance, then the expected value of $\chi^2 = (\chi^2_{dir} + \chi^2_{mag})/3$ will be 1. We define the parameter uncertainty σ_ρ such that the change from ρ_0 to $\rho_0 + \sigma_\rho$ causes the mean model value B_i^M to go to $B_i^M + \sigma_B$, where σ_B is defined as the width of the observation random variable, unity. The expected value of χ^2_{dir} becomes 2 and $\Delta\chi^2 = 1$ corresponds to a 1 σ_B change in the mean model value for every data point. The average σρ to cause this change was $\langle\sigma_\rho\rangle = 0.22 \pm 0.10$. The assumption that our observations are distributed as a Gaussian about the model value is one of convenience, although on the scale of the normalized fields the error width is quite large.

[32] Recently, *Lepping et al.* [2002] have investigated this issue of the uncertainties in the best fit parameters by running Monte Carlo simulations of trend noise derived

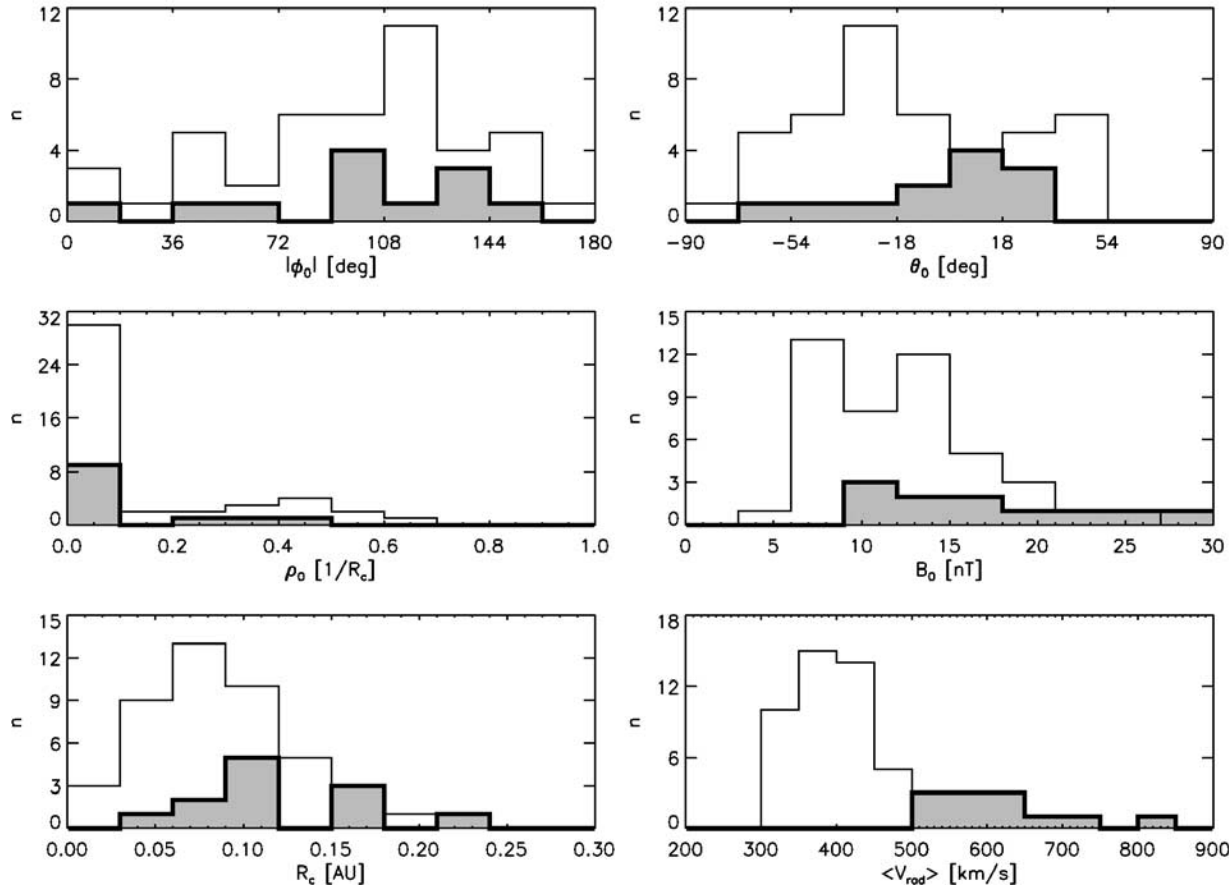

Figure 4. Histogram distributions of the model parameters, $|\phi_o|$, θ_o, ρ_o, B_o, R_c, and the average cloud velocity $\langle V_{rad} \rangle$. The thin outlined bars indicate slow clouds, $\langle V_{rad} \rangle < 500$ km/s, and the thick gray bars represent fast clouds, $\langle V_{rad} \rangle \geq 500$ km/s. These distributions are summarized in Table 2 and discussed in section 3.3.

from data. For "medium" to "high" noise conditions they obtained uncertainties for ϕ_0 and θ_0 on the order of 10–20 degrees and a value of $\sigma_\rho \sim 0.2$–0.3. While our approach is quite different, we obtain almost identical results for the estimate of $\langle \sigma_\rho \rangle$.

4. Magnetic Clouds During the Solar Cycle

4.1. Axial Current and Toroidal Flux

[33] From the model geometry and the cylinder fit parameters we can derive the total axial current and the toroidal (or axial) magnetic flux of these clouds. Both quantities are related to the cloud radius and axial field strength model parameters, $I_z \propto B_0 R_c$ and $\Phi_z \propto B_0 R_c^2$. The marginal differences between slow and fast magnetic clouds seen in the average field strength and cloud size model parameters are slightly more apparent in the current and flux distributions but perhaps still not statistically significant. These calculations rely heavily on the model geometry and are therefore the roughest of estimates and probably a lower bound. The multipoint observations of *Mulligan and Russell* [2001] imply an elliptic cross-section with a 4:1 ratio suggesting a factor of 4 would be required to correct the flux derived from the cylindrical model.

[34] The top panel of Figure 5 shows the axial current distribution plotted against the logarithm of current in Amps. The outlined bars are slow clouds; the gray bars are fast clouds in the style of Figure 4. The lower panel is the distribution of logarithmic toroidal magnetic flux passing through the circular cloud cross section.

[35] The role magnetic clouds play in the reconfiguration of the solar global field is surely related to flux transport from the Sun into the heliosphere. Figure 6 shows the cumulative total toroidal magnetic flux as a function of time added to the heliosphere from our observed magnetic cloud events at 1 AU. The toroidal flux transported by the

Table 2. Average Model Parameter/Physical Quantity Values

Parameter/Quantity	Slow Clouds	Fast Clouds
Number of events	44	12
$\lvert\phi_0\rvert$	108 ± 49 deg	105 ± 48 deg
θ_0	−6 ± 40 deg	8 ± 34 deg
ρ_0	0.14 ± 0.21	0.10 ± 0.18
B_0	12.3 ± 4.7 nT	19.3 ± 9.7 nT
R_c	0.086 ± 0.041 AU	0.121 ± 0.049 AU
$\langle V_{rad} \rangle$	392 ± 46 km/s	616 ± 97 km/s
Δt	22.7 ± 8.0 hours	21.3 ± 6.7 hours
I_z	$4.30 \pm 2.62 \times 10^8$ A	$10.0 \pm 6.45 \times 10^8$ A
Φ_z	$3.67 \pm 3.76 \times 10^{20}$ Mx	$11.7 \pm 11.1 \times 10^{20}$ Mx

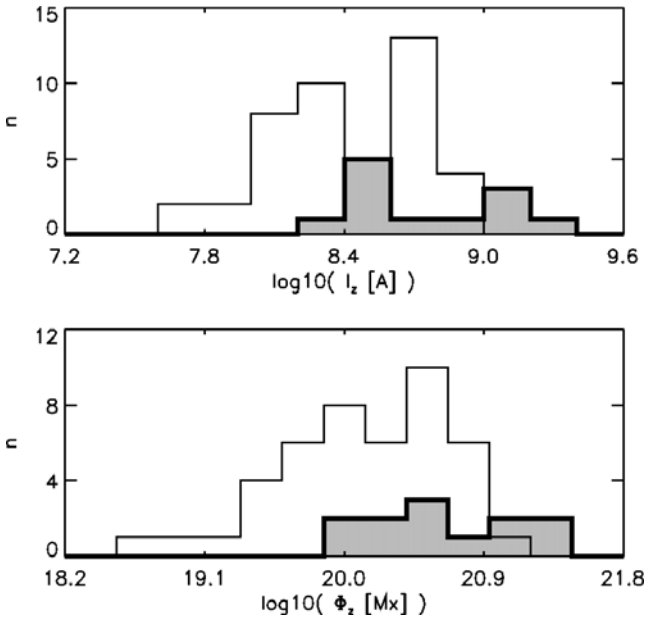

Figure 5. (top) The histogram distribution of the total logarithmic axial current in Amps, in the same style as Figure 4. (bottom) The distribution of total logarithmic axial (toroidal) magnetic flux in Maxwells.

fast magnetic clouds (21% of events) is equal to 46.5% of the total.

[36] These magnetic clouds are responsible for adding an $\sim 8.6 \times 10^{21}$ Mx/yr during our selected time period. If we assume this rate is constant then magnetic clouds would produce $\sim 10^{23}$ Mx of toroidal magnetic flux over the 11-year solar cycle. If magnetic clouds are 33% of all CMEs, then the total toroidal flux transported by CMEs is three times that. This estimate is fairly consistent with the *Bieber and Rust* [1995] estimate of 10^{24} Mx of total toroidal flux shed over the solar cycle. Much closer agreement would be obtained by correcting for elliptic flux rope cross-sections. Since the continuing build up of flux in the heliosphere is not observed, there must be ongoing magnetic reconnection processes negating the "flux catastrophe." This magnetic reconnection could be between closed-closed, open-open, or open-closed field lines. Open-closed interchange reconnection and its effect on ICME evolution is an area of ongoing study [*McComas et al.*, 1995; *Crooker et al.*, 2001; *Reinard et al.*, 2002].

4.2. Evolution of Magnetic Orientation

[37] The 3 1/2 years of ACE data used in this study include the rising phase and most of the solar maximum of cycle 23. *Bothmer and Rust* [1997] argue that the leading polarity of magnetic clouds should follow the overall dipolar field of the Sun. *Mulligan et al.* [1998] showed this to be true by examining magnetic cloud orientations in 9 years of Pioneer Venus Orbiter (PVO) data. However, there appears to be differences in the orientation solar cycle dependence of magnetic clouds associated with quiescent or polar crown filaments and those associated with active region sigmoid eruptions [*Leamon et al.*, 2002].

[38] *Mulligan et al.* [1998] used eight classifications for the magnetic field orientation, combining the systems used by *Bothmer and Rust* [1997], *Bothmer and Schwenn* [1998], and *Zhao and Hoeksema* [1996]. These classifications address the magnetic field rotations in the plane perpendicular to the sun-spacecraft line (approximately the T-N plane in Figure 2 or the Y-Z plane in GSE coordinates). Therefore this classification scheme only depends on the magnetic field model implicitly and the full three-dimensional cylinder orientation is not needed.

[39] The clouds with cylinder axes that lie approximately in the ecliptic plane are called bipolar clouds because the z-component of the magnetic field will change sign during the event passage. North-south clouds have leading $B_z > 0$ and trailing $B_z < 0$ and are called NES or NWS depending on the sign of B_y, South-north clouds (SEN, SWN) are the opposite ($B_z < 0$ followed by $B_z > 0$). Unipolar clouds have their axis highly inclined with respect to the ecliptic and thus have a single signed B_z value. There are four unipolar categories corresponding to east-west (ENW, ESW) and west-east (WNE, WSE) cloud orientations, describing the leading, trailing sign of B_y. From the fit parameters in Table 1 we see that the unipolar clouds typically have $|\theta_0| > 30°$ and small ρ_0.

[40] These eight orientation categories classify a vast majority of the cloud events, however a small number of our clouds were not easily identifiable as belonging to any one of these categories, i.e., their rotations projected onto the Y-Z plane did not fulfill all the requirements given by *Mulligan et al.* [1998]. These cases are indicated in Table 1 with a question mark (?). To classify these orientations, we "rounded" using a combination of the data and the model fits.

[41] The handedness or chirality of the magnetic field rotations in the Y-Z plane can be determined from the model fit parameters ϕ_0 and H with the formula

$$C = \mathrm{sgn}(\sin\phi_0) \cdot H, \tag{5}$$

such that C is +1 for clouds with right handed Y-Z rotations and -1 for left handed Y-Z rotations. The right handed Y-Z

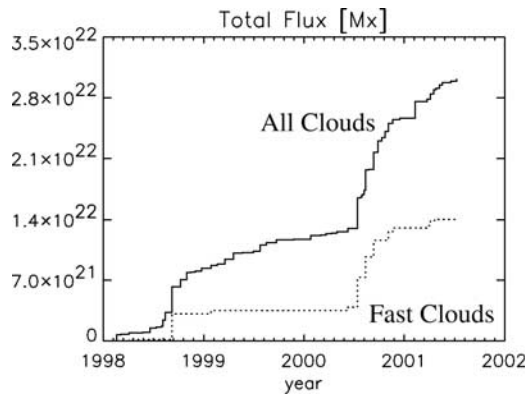

Figure 6. The total cumulative toroidal magnetic flux carried by magnetic cloud ICMEs observed at 1 AU. The fast cloud contribution is ~46% of the total flux while being only 21% of the events.

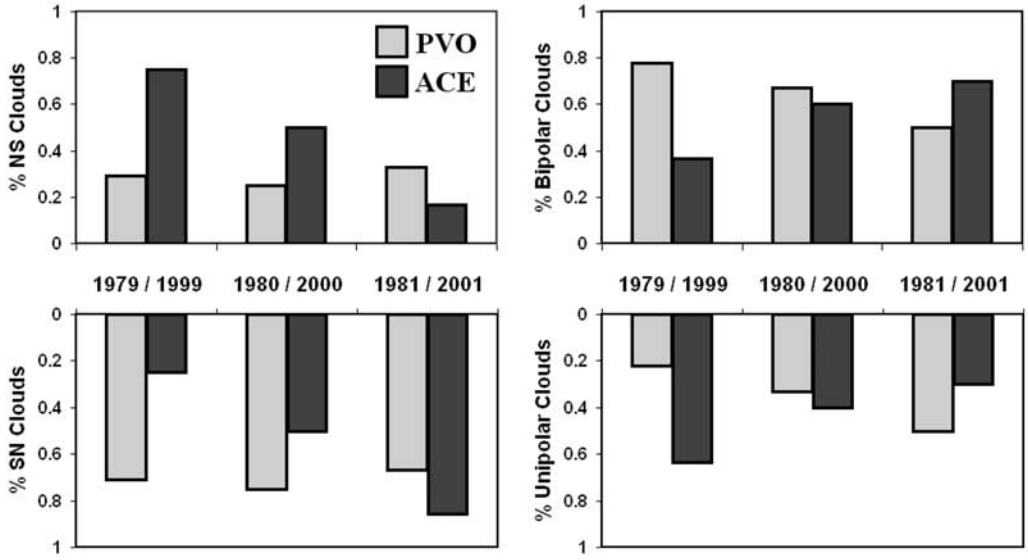

Figure 7. (left) A comparison of the evolution of the distribution of bipolar (N-S, S-N) oriented clouds during solar maximum of cycles 21 (PVO) and 23 (ACE). (right) The evolution of the number of the unipolar and bipolar cloud orientations during solar maximum. The ACE data appears to have the opposite trends in both plots. The 2001 bar only includes data through July. PVO data adapted from *Mulligan et al.* [1998].

rotations are SWN, NES, ESW, and WNE. The ϕ_0 values of 0.0 and 180.0 in Table 1 are rounded to a single decimal place, so equation (5) always gave ±1.

[42] Figure 7 compares our magnetic orientation evolution during the maximum of solar cycle 23 seen by ACE and the evolution during the same time period in solar cycle 21 seen by PVO as presented by *Mulligan et al.* [1998]. The histograms are normalized for ease of comparison between the two data sets, and we note that 2001 only represents 7 months of data rather than a full year. Solar maximum of cycle 21 was 1979–1981 while solar maximum for cycle 23 was approximately 1999–2001 with a slight indication of a double peak. The ACE data do not show much agreement. The bipolar clouds are predominately S-N during cycle 21, yet ACE saw many N-S clouds in 1999 and 2000. The trend in the number of bipolar and unipolar clouds also seems to be in mild disagreement between the ACE and PVO data, their slopes look equal and opposite over the three years of solar maximum. For a more complete comparison of the solar cycle evolution, a much longer period of ACE data is needed and will be the subject of future work.

5. Plasma and Composition Spatial Structure

5.1. Spatial Mapping Procedure

[43] Figure 8 depicts our general procedure for extracting composition spatial structure from the magnetic field model. The upper panel shows the spacecraft trajectory through the cloud projected onto the plane perpendicular to the cloud axis. Using the model geometry, we are able to associate any ACE measured quantity $Q(t)$ with a radial distance $\rho(t)$ inside the model cylinder. This defines a simple mapping to determine the spatial dependence, $Q(\rho(t))$. It is important to notice that the distances $\rho(t)$ from the axis in the projected spacecraft trajectory are always symmetric around the impact parameter ρ_0 of the model fit. We allow the mapping to be asymmetric by taking the distances earlier in time to be negative. The incoming half is $\rho < 0$ and the outgoing half is $\rho > 0$. This ensures that any consistent, structural differences between the leading and trailing halves of the events will be maintained during the profile averaging. This effect is demonstrated in the lower panel of Figure 8 where the spatial sampling starts at $\rho = -1$ and ends at $\rho = +1$. By applying this procedure to our entire set of cloud events we are able to construct a composite statistical average of a full diameter cut of any measured ACE quantity.

5.2. Results

[44] Figure 9 is a collection of these diameter profiles for both slow and fast clouds. The slow cloud profiles are indicated by the dashed line connecting error bars and the fast cloud profiles are solid lines connecting triangles. We used 15 bins to divide the diameter cut and computed the average value in each bin. The vertical error bars are the standard deviation of the mean in each bin. The horizontal error bars represent the histogram bin width. The bin width is 0.133 of the normalized cloud radius and represents the maximum statistical scatter in radial distance in each bin. However, this 7% independent statistical error does not include the ~20% systematic model uncertainty of the parameter ρ_0 described in section 3.4. All of the major structural trends, particularly the relative levels of enhancement are still present when taking this systematic model error into account.

[45] The bins closer to the cloud edges have more data points than the bins in the center of the cloud because of the mapping procedure. Owing to various gaps in the level 2 data (indicated on Table 1), the number of data points per bin are not symmetric in ρ nor the same for the different quantities.

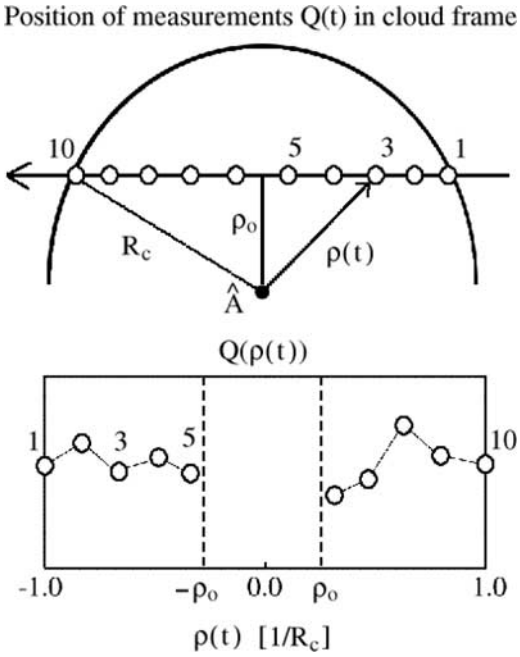

Figure 8. (top) The spacecraft trajectory in the cloud frame, showing the positions of a measured quantity $Q(t)$ during the cloud event. (bottom) A plot of the inferred position structure, $Q(\rho(t))$, within the magnetic cloud. Notice the incoming/outgoing asymmetry remains intact and that time runs left to right along the ρ axis. The ρ axis is normalized by cloud radius, R_c, such that we can look for common structure among clouds of different sizes.

[46] The first plot is the average radial velocity $\langle V_{rad} \rangle$. The slow cloud velocity profile has the typical shape characteristic of a magnetic cloud where the slight negative slope is due to the cloud expansion. The fast cloud velocity profile has the same large scale trend but is less smooth. This is an indication of fewer data points as well as a larger variability than the slow cloud events.

[47] The proton temperature is essentially symmetric in ρ, with the fast clouds showing much more variation as well as a trend of being hotter toward their edges. The average dip seen in both the fast and slow profiles is most likely explained by the low proton temperature event selection criteria. A possibility for the stronger leading edge temperatures in the fast cloud profile may be the interaction with the slower upstream solar wind.

[48] The proton density profiles appear to be almost symmetric. The slow clouds seem to show a smooth 20% decrease toward the center. The fast clouds are less dense throughout, decrease rapidly from the edges, and show a symmetric increase toward the center. The slow solar wind has an average $N_p \sim 10$ cm^{-3} with considerable variation of around 40% [*Schwenn*, 1990]. The fast magnetic clouds are depleted compared to the "average" slow solar wind. This might be expected from the familiar anticorrelation between solar wind speed and density, however the internal structure is of more interest to us. While the error bars are fairly large, the fast cloud profile does seem to indicate a slightly denser center, consistent with the idea of an "average" three-part CME structure inferred from coronagraph observations [e.g., *Illing and Hundhausen*, 1986].

[49] The alpha to proton ratio profiles are very similar for fast and slow events. The slow cloud N_α/N_p ratio increase slowly toward the rear of the cloud. The fast cloud ratio increases, levels off and becomes more variable, meeting the slow cloud profile, and shows a prominent average spike at three-fourths of the way through the cloud. This spike is enhanced due to a particularly helium enriched event (day 268, 1998). Removing this contribution brings the bin average down to ~0.08, which becomes only a modest enhancement over the slow cloud value. The N_α/N_p ratio is highly variable in the slow solar wind and ICME identification is usually based on $N_\alpha/N_p > 0.08-0.10$ [*Borrini et al.*, 1981, 1982]. While our "average" magnetic cloud profiles do not meet this enhancement criteria, certainly some individual events do so.

[50] The oxygen and iron charge states of both velocity classes are enhanced relative to long term averages over the highly variable slow solar wind. *Zurbuchen et al.* [2000] found $\langle O^{7+}/O^{6+} \rangle = 0.39 \pm 0.13$ in the slow solar wind. *Lepri et al.* [2001] found that extended periods of $Fe^{\geq 16+}/Fe_{total} \geq \sim 0.10$ had anywhere from an 80–100% overlap with ICME periods depending on the ICME identifying characteristics, e.g., bidirectional electrons. In the 2-hour iron data averages used by Lepri et al. the non-CME associated slow solar wind had $Fe^{\geq 16+}/Fe_{total}$ values that did not deviate statistically from zero.

[51] The oxygen and iron charge state ratios have qualitatively different diameter profiles. On average, they both show that the faster clouds have higher charge states, but this is much less obvious in the O^{7+}/O^{6+} profiles where the diameter average is ~1.0 for slow clouds and ~1.5 for fast clouds. Both of the O^{7+}/O^{6+} profiles show significant variation. The large error bar on the $\rho = 0.5$ spike indicates a single anomalously high point dominating the bin average (also from the day 268, 1998 event). The $Fe^{\geq 16+}/Fe_{total}$ profiles show a relatively smooth, symmetric peak at the center of the cloud for the slow average profile, and perhaps a noisier version of the same trend for the fast profile. The differences between iron charge states are quite striking, especially compared to the similarities of the N_α/N_p and O^{7+}/O^{6+} profiles. The heavy oxygen and iron charge state ratios can be used to derive coronal electron temperatures for a given expansion time and spatial scales in the region of charge state freeze-in close to the Sun.

[52] We have examined the robustness of these average profiles in light of the ability of a single event to weight bin averages in both the N_α/N_p and O^{7+}/O^{6+} profiles. We excluded all of the poor cylinder model fits ($\chi^2_{dir} > 0.20$ in Table 1) and found that the plasma and composition profiles looked remarkably similar. This had the effect of removing 15 slow cloud events and 3 fast cloud events from the profile averages. All of the slow cloud profiles were essentially identical, with the largest change being an almost uniform decrease in the N_p profile of ~0.5 cm^{-3}. The fast cloud average profile changes were within 1 σ of the old values with the following exceptions. The central peak in the fast cloud N_p profile became much less prominent but was still enhanced compared to the symmetric dips. The O^{7+}/O^{6+} profile showed slightly more enhancement over the

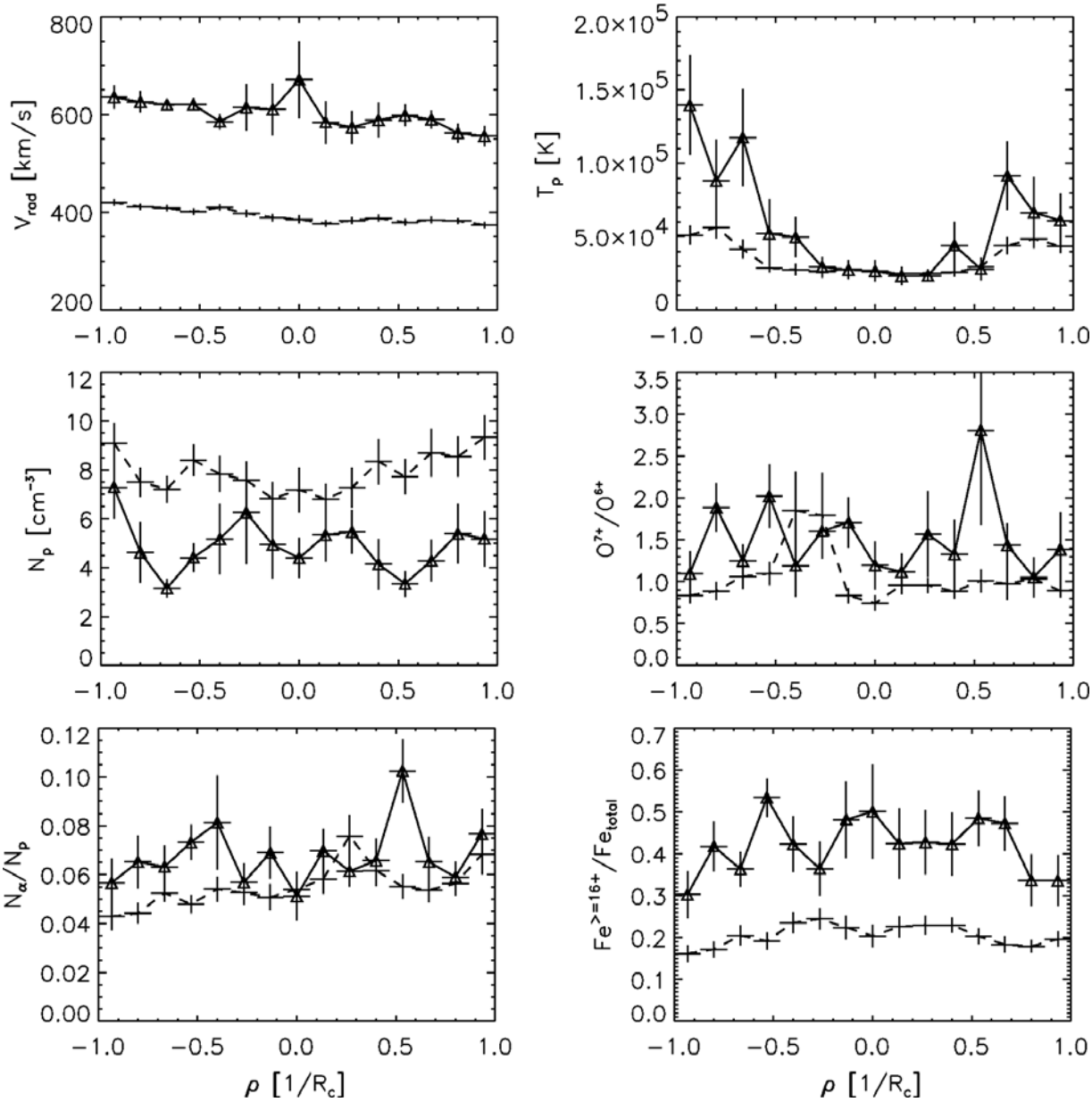

Figure 9. Diameter cuts through composite statistical averages of the mean radial velocity $\langle V_{rad} \rangle$, proton temperature T_p, proton density N_p, the oxygen charge state ratio O^{7+}/O^{6+}, the alpha to proton ratio N_α/N_p, and high iron charge state ratio $Fe^{\geq 16+}/Fe_{total}$. The ρ-axis is normalized cloud radius, with ρ = −1.0 indicating the incoming edge, +1.0 the outgoing edge. $\langle V_{rad} \rangle < 500$ km/s is plotted as a dashed line connecting the error bars, $\langle V_{rad} \rangle \geq 500$ km/s is plotted as solid line connecting triangles. The vertical error bars are the standard deviation of the mean in each bin, the horizontal error bars are the bin width.

slow cloud values and less variation in the first half of the profile.

6. Discussion

[53] We have presented the most complete set of ACE magnetic cloud observations to date. All of our results indicate a significant difference between slow and fast magnetic clouds. Magnetic cloud events are of particular interest because of their potential role in the large scale magnetic field evolution of the Sun and their implied constraints on the physical processes of flux rope CME origin.

[54] The faster clouds are not only characterized by marginally greater flux, but more importantly, they have different plasma and ionic composition signatures. The fast clouds have lower proton density and are more enhanced in N_α/N_p in the first half of the cloud. The oxygen and iron charge states are also increased throughout fast clouds, which is a good indication of a hotter coronal electron temperature. It appears that most of these features are related in a consistent way, having to do with overall

energy of the solar environment of the CME origin. We observe more energy in fast clouds at 1 AU (both kinetic and magnetic) as well as evidence for a heated coronal environment.

[55] One obtains an estimate of the electron temperature in the corona from the heavy ion charge state observations by equating the expansion time scale to the equilibrium time scale of the individual ion species. This expansion time scale can be defined as a characteristic scale height divided by the velocity of the plasma near the Sun. To compare our slow and fast magnetic clouds we take 1 $R_{\odot}$ as the scale height and velocity estimates typical of speeds inferred from coronagraph observations for the two types of CME acceleration profiles. In general, slow CMEs speed up and fast CMEs slow down, so the relationship between observed ICME speeds at 1 AU and coronagraph CME speeds is much more complicated than a simple one-to-one correspondence. A rigorous treatment must include the properties of the ambient solar wind and the interaction between the ejecta and this background. That being said, if we assume slow and fast coronagraph speeds of 200 km/s and 1000 km/s [e.g., *Sheeley et al.*, 1999] are characteristic for our slow and fast magnetic cloud events near the Sun, then the electron temperatures from the diameter averaged O^{7+}/O^{6+} ratios of 1.0 for slow clouds and 1.5 for fast clouds are $\sim 2.0 \times 10^6$ K and $\sim 2.3 \times 10^6$ K, respectively. These temperatures also correspond to freeze-in electron densities of $\sim 1.3 \times 10^8$ cm^{-3} for slow clouds and $\sim 4.3 \times 10^8$ cm^{-3} for fast clouds.

[56] The difference in electron temperature implies an increase of 15% in internal energy in fast magnetic clouds. However, these estimates assume a steady state flow speed which is not exactly applicable to transient events. A more complete treatment of the electron temperature and density inversions with realistic CME expansion timescales will be addressed in future work.

[57] Our results could be used to constrain some of the models currently being used to describe magnetic clouds and flux rope CMEs. There are two schools of thought on the origins of flux rope CMEs; either the helical flux rope structure was preexisting in quasi-equilibrium and erupted via some mechanism, or the helical flux rope structure was generated during the eruption process (see review by *Klimchuk* [2001]). Many of these models have been compared to white-light coronagraph images and there has been relatively good agreement in reproducing general CME features [e.g., *Gibson and Low*, 1998; *Chen et al.*, 2000; *Manchester et al.*, 2002]. However, if these CME events are also the magnetic clouds seen in the heliosphere, then the same simulations must also reproduce the observed spacecraft measurements.

[58] The quantities commonly simulated for comparison with in situ observations are the vector magnetic field, proton density and temperature, and cloud velocity. These tend to match the observed properties of magnetic clouds at least qualitatively [*Wu et al.*, 1999; *Krall et al.*, 2000; *Linker et al.*, 2002]. In working toward quantitative agreement, composition profiles could be included in this convergence. This would challenge the modelers of CME initiation to produce electron temperatures and densities at the sun consistent with the observed ionic charge states in the interior of their erupting flux rope.

[59] The correct model should also describe the compositional differences between fast and slow magnetic clouds. There is a perhaps a precedence for two separate types of CMEs characterized by their velocity profiles in coronagraph observations and the location of their origin. *Low and Zhang* [2002] presented a theoretical framework for two topologically different origins having to do with the filament orientation polarity with respect to the background field. It is not obvious that the different resulting flux rope topologies from ''inverse'' and ''normal'' filament eruptions would evolve into the similar magnetic structures with differing plasma histories, as observed at 1 AU.

[60] It is important to remember that all of our spatial structure is derived from the application of the static, linear, force-free magnetic field model. To the extent that this model correctly describes the three-dimensional magnetic structure of the flux rope, our spatial structure is valid. The true ρ_0 parameter uncertainty, even rigorously defined, is still only an error within the framework of the assumed magnetic field model. While there exists a physical reason to believe the fields may be evolving toward a force-free state, by no means are we certain that ''complete'' internal reconnection has provided a linear force-free configuration by 1 AU.

[61] It would be interesting to compare similar spatial mapping analyses for different flux rope magnetic field models. One suspects that any symmetric model would yield similar results to those presented here. Some of the newer, more complicated models are not symmetric and thus probably better describe reality. For example, the *Russell and Mulligan* [2002] elliptical flux rope geometry has three different length scales and the flux rope solutions to the Grad-Shafranov equation using the spacecraft data as a boundary condition are neither symmetric nor force-free [*Hu and Sonnerup*, 2001]. It may be that a nonsymmetric spatial structure, derived from a complicated field model, would show many of the features presented here. However, it would be much harder to compare multiple events, or construct an average profile, if the physical geometry of the flux ropes were different every time.

7. Conclusion

[62] We have presented an analysis of 56 magnetic clouds events observed by the ACE spacecraft near the maximum of solar cycle 23. Applying the simplest static, linear, force-free magnetic field model and a successful fitting technique, we have shown general agreement with previous statistical surveys and their model parameter distributions. Using the geometry inherent in the static magnetic field model, we have mapped various plasma and composition quantities to a distance from the cylindrical model axis. This enabled us to build up mean composition distributions along the diameter of the model cylinder.

[63] The internal plasma and composition profiles suggest two classes or origins of magnetic clouds. We have motivated this analysis by briefly discussing the application of these results to the transport of toroidal magnetic flux by these well-ordered CMEs into the heliosphere. We have also suggested some constraints these compositional profiles could place on various aspects of the modern flux rope modeling effort. This includes coronal electron temperatures and densities required to reproduce our observed charge

states at 1 AU as well as the ability to generate two distinct classes of flux rope CMEs with almost identical magnetic topologies at 1 AU.

[64] **Acknowledgments.** The authors would like to thank C. Smith, R. Skoug, and the MAG and SWEPAM teams, respectively, for preparation of the level 2 data available on the ACE Science Center website (http://www.srl.caltech.edu/ACE/ASC/) as well as A. Reinard and S. Lepri for assistance with the oxygen and iron charge state data. BJL also thanks D. Rust for helpful discussion about flux and helicity and acknowledges student travel support for the 2002 NSF SHINE meeting. This work was supported in part by ONR and NASA.

[65] Shadia Rifai Habbal thanks Ruth M. Skoug and another referee for their assistance in evaluating this paper.

References

Bame, S. J., J. R. Asbridge, W. C. Feldman, E. E. Fenimore, and J. T. Gosling, Solar wind heavy ions from flare heated coronal plasma, *Solar Phys.*, *62*, 179, 1979.

Bieber, J. W., and D. M. Rust, The escape of magnetic flux from the sun, *Astrophys. J.*, *453*, 911, 1995.

Borrini, G., J. M. Wilcox, J. T. Gosling, S. J. Bame, and W. C. Feldman, Solar wind helium and hydrogen structure near the heliospheric current sheet—A signal of coronal streamers at 1 AU, *J. Geophys. Res.*, *86*, 4565, 1981.

Borrini, G., J. T. Gosling, S. J. Bame, and W. C. Feldman, Helium enhancements in the solar wind, *J. Geophys. Res.*, *87*, 7370, 1982.

Bothmer, V., and D. M. Rust, The field configuration of magnetic clouds and the solar cycle, in *Coronal Mass Ejections*, *Geophys. Monogr. Ser.*, vol. 99, edited by N. Crooker, J. A. Joselyn, and J. Feynmann, p. 139, AGU, Washington, D. C., 1997.

Bothmer, V., and R. Schwenn, Eruptive prominences as sources of magnetic clouds in the solar wind, *Space Sci. Rev.*, *70*, 215, 1994.

Bothmer, V., and R. Schwenn, The structure and origin of magnetic clouds in the solar wind, *Ann. Geophys.*, *16*, 1, 1998.

Bürgi, A., and J. Geiss, Helium and minor ions in the corona and solar wind: Dynamics and charge states, *Solar Phys.*, *103*, 347, 1986.

Burlaga, L. F., Magnetic clouds and force-free fields with constant alpha, *J. Geophys. Res.*, *93*, 7217, 1988.

Burlaga, L. F., Magnetic clouds, in *Physics of the Inner Heliosphere*, vol. 2, edited by R. Schwenn and E. Marsch, p. 1, Springer Verlag, New York, 1991.

Burlaga, L. F., et al., A magnetic cloud containing prominence material: Janurary 1997, *J. Geophys. Res.*, *103*, 277, 1998.

Cane, H. V., I. G. Richardson, and G. Wibberenz, Helios 1 and 2 observations of particle decreases, ejecta, and magnetic clouds, *J. Geophys. Res.*, *102*, 7075, 1997.

Chen, J., et al., Magnetic geometry and dynamics of the fast coronal mass ejection of 1997 September 9, *Astrophys. J.*, *533*, 481, 2000.

Crooker, N. U., S. W. Kahler, and J. T. Gosling, Reducing heliospheric magnetic flux from CMEs without disconnection, *Eos Trans. AGU*, *82*(20), Spring Meet. Suppl., Abstract SH51C-04, 2001.

Dere, K. P., G. E. Brueckner, R. A. Howard, D. J. Michels, and J. P. Delaboudiniere, Lasco and EIT observations of helical structure in coronal mass ejections, *Astrophys. J.*, *516*, 465, 1999.

Esser, R. E., and R. J. Edgar, Reconciling spectroscopic electron temperature measurements in the solar corona with in situ charge state observations, *Astrophys. J.*, *532*, L71, 2000.

Fenimore, E. E., Solar wind flows associated with hot heavy ions, *Astrophys. J.*, *235*, 245, 1980.

Galvin, A. B., Minor ion composition in CME-related solar wind, in *Coronal Mass Ejections*, *Geophys. Monogr. Ser.*, vol. 99, edited by N. Crooker, J. A. Joselyn, and J. Feynmann, p. 253, AGU, Washington, D. C., 1997.

Geiss, J., G. Gloeckler, and R. von Steiger, Origin of the solar wind from composition data, *Space Sci. Rev.*, *72*, 49, 1995.

Gibson, S. E., and B. C. Low, A time-dependent three-dimensional magnetohydrodynamic model of the coronal mass ejection, *Astrophys. J.*, *493*, 460, 1998.

Gloeckler, G., et al., The Solar Wind Ion Composition Spectrometer, *Astron. Astrophys. Suppl. Ser.*, *92*, 267, 1992.

Gloeckler, G., et al., Investigation of the composition of solar and interstellar matter using solar wind and pickup ion measurements with SWICS and SWIMS on the ACE spacecraft, *Space Sci. Rev.*, *86*, 497, 1998.

Gloeckler, G., et al., Unusual composition in the solar wind in the 2–3 May 1998 CME observed with SWICS on ACE, *Geophys. Res. Lett.*, *26*, 157, 1999.

Goldstein, H., On the field configuration in magnetic clouds, in *Solar Wind Five*, edited by M. Neugebauer, *NASA Conf. Publ., CP-2280*, 731, 1983.

Gosling, J. T., Coronal mass ejections and magnetic flux ropes in interplanetary space, in *Physics of Magnetic Flux Ropes*, *Geophys. Monogr. Ser.*, vol. 58, edited by C. T. Russell, E. R. Priest, and L. C. Lee, p. 9, AGU, Washington, D. C., 1990.

Henke, T., et al., Differences in O^{7+}/O^{6+} ratio of magnetic cloud and non-cloud coronal mass ejections, *Geophys. Res. Lett.*, *25*, 3465, 1998.

Henke, T., et al., Ionization state and magnetic topology of coronal mass ejections, *J. Geophys. Res.*, *106*, 10,957, 2001.

Hu, Q., and B. U. Ö. Sonnerup, Reconstruction of magnetic flux ropes in the solar wind, *Geophys. Res. Lett.*, *28*, 467, 2001.

Illing, R. M. E., and A. J. Hundhausen, Disruption of a coronal streamer by an eruptive prominence and coronal mass ejection, *J. Geophys. Res.*, *90*, 10,951, 1986.

Klimchuk, J. A., Theory of coronal mass ejections, in *Space Weather*, *Geophysical Monogr. Ser.*, vol. 125, edited by P. Song, H. J. Singer, and G. L. Siscoe, p. 143, AGU, Washington, D. C., 2001.

Krall, J., J. Chen, and R. Santoro, Drive mechanisms of erupting solar magnetic flux ropes, *Astrophys. J.*, *539*, 964, 2000.

Leamon, R. J., R. C. Canfield, and A. A. Pevtsov, Properties of magnetic clouds and geomagnetic storms associated with eruption of coronal sigmoids, *J. Geophys. Res.*, *107*(A9), 1234, doi:10.1029/2001JA000313, 2002.

Lepping, R. P., J. A. Jones, and L. F. Burlaga, Magnetic field structure of interplanetary magnetic clouds at 1 AU, *J. Geophys. Res.*, *95*, 11,957, 1990.

Lepping, R. P., et al., Can estimating errors in force free magnetic cloud model fit-parameters be fun?, *Eos. Trans. AGU*, *83*(19), Spring Meet. Suppl., Abstract SH22D-09, 2002.

Lepri, S. T., et al., Iron charge distribution as an identifier of interplanetary coronal mass ejections, *J. Geophys. Res.*, *106*, 29,231, 2001.

Linker, J. A., Z. Mikic, P. Riley, R. Lionello, and D. Odstricil, CME evolution in the corona and solar wind, *Eos. Trans. AGU*, *83*(47), Fall Meet. Suppl., Abstract SH61A-0433, 2002.

Low, B. C., and M. Zhang, The hydromagnetic origin of the two dynamical types of solar coronal mass ejections, *Astrophys. J.*, *564*, L53, 2002.

Lundquist, S., Magnetohydrostatic fields, *Ark. Fys*, *2*, 361, 1950.

Lust, R., and A. Schluter, Force-free magnetic fields, *Z. Astrophys.*, *34*, 353, 1954.

Manchester, W. B., IV, et al., 3-D MHD simulation of CME propagation from solar corona to 1 AU, *Eos. Trans. AGU*, *83*(47), Fall Meet. Suppl., Abstract SH21A-0501, 2002.

McComas, D. J., et al., Solar Wind Electron Proton Alpha Monitor (SWEPAM) for the Advanced Composition Explorer, *Space Sci. Rev.*, *86*, 563, 1998.

McComas, D. J., et al., Reconnection on open field lines ahead of coronal mass ejections, *Space Sci. Rev.*, *72*, 129, 1995.

Mulligan, T., C. T. Russell, and J. G. Luhmann, Solar cycle evolution of the structure of magnetic clouds in the inner heliosphere, *Geophys. Res. Lett.*, *25*, 2959, 1998.

Mulligan, T., and C. T. Russell, Multispacecraft modeling of the flux rope structure of interplanetary coronal mass ejections: Cylindrically symmetric versus nonsymmetric topologies, *J. Geophys. Res.*, *106*, 10,581, 2001.

Owocki, S. P., and J. D. Scudder, The effect of a non-maxwellian electron distribution on oxygen and iron ionization balances in the solar corona, *Astrophys. J.*, *270*, 758, 1983.

Plunkett, S. P., et al., Simultaneous SOHO and ground-based observations of a large eruptive prominence and coronal mass ejection, *Sol. Phys.*, *194*, 371, 2000.

Reinard, A. A., et al., Comparison between average charge states and abundances of ions in CMEs and the slow wind, in *Solar and Galactic Composition; Joint SOHO/ACE Workshop*, edited by R. F. Wimmer-Schweingruber, *AIP Conf. Proc., 598*, 139, 2001.

Reinard, A. A., L. A. Fisk, and T. H. Zurbuchen, A model decribing the reconnection of magnetic field lines behind coronal mass ejections, *Eos. Trans. AGU*, *83*(19), Spring Meet. Suppl., Abstract SH32D-02, 2002.

Richardson, I. G., and H. V. Cane, Regions of abnormally low proton temperature in the solar wind (1965–1991) and their association with ejecta, *J. Geophys. Res.*, *100*, 23,397, 1995.

Russell, C. T., and T. Mulligan, The true dimensions of interplanetary coronal mass ejections, *Adv. Space Res.*, *29*, 301, 2002.

Rust, D. M., Spawning and shedding of helical magnetic fields in the solar atmosphere, *Geophys. Res. Lett.*, *21*, 241, 1994.

Rust, D. M., Magnetic helicity in solar filaments and coronal mass ejections, in *Magnetic Helicity in Space and Laboratory Plasmas*, *Geophys. Monogr. Ser.*, vol. 111, edited by M. R. Brown, R. C. Canfield, and A. A. Pevtsov, p. 221, AGU, Washington, D. C., 1999.

Schwenn, R., H. Rosenbauer, and K.-H. Muehlhaeuser, Singly-ionized helium in the driver gas of an interplanetary shock wave, *Geophys. Res. Lett.*, *7*, 201, 1980.

Schwenn, R., Large-scale structure of the interplanetary medium, in *Physics of the Inner Heliosphere*, vol. 1, edited by E. Schwenn and E. Marsch, pp. 99–181, Springer-Verlag, New York, 1990.

Sheeley, N. R., Jr., J. H. Walters, Y.-M. Wang, and R. A. Howard, Continuous tracking of coronal outflows: Two kinds of coronal mass ejections, *J. Geophys. Res.*, *104*, 24,739, 1999.

Shimazu, H., and K. Marubashi, New method for detecting interplanetary flux ropes, *J. Geophys. Res.*, *105*, 2365, 2000.

Skoug, R. M., et al., A prolonged He+ enhancement within a coronal mass ejection in the solar wind, *Geophys. Res. Lett.*, *26*, 161, 1999.

Smith, C. W., et al., The ACE magnetic field experiment, *Space Sci. Rev.*, *86*, 613, 1998.

von Steiger, R., et al., Composition of quasi-stationary solar wind flows from Ulysses/Solar Wind Ion Composition Spectrometer, *J. Geophys. Res.*, *105*, 27,217, 2000.

Wu, S. T., W. P. Guo, D. J. Michels, and L. F. Burlaga, MHD description of the dynamical relationships between flux rop, streamer, coronal mass ejection, and magnetic cloud: An analysis of the January 1997 Sun-Earth connection event, *J. Geophys. Res.*, *104*, 14,789, 1999.

Zhao, X., and J. T. Hoeksema, Effect of coronal mass ejections on the structure of the heliospheric current sheet, *J. Geophys. Res.*, *101*, 4825, 1996.

Zurbuchen, T. H., S. Hefti, L. A. Fisk, G. Gloeckler, and N. A. Schwadron, The magnetic structure of the slow solar wind: Constraints from composition data, *J. Geophys. Res.*, *105*, 18,327, 2000.

Zurbuchen, T. H., L. A. Fisk, G. Gloeckler, and R. von Steiger, The solar wind composition throughout the solar cycle: A continuum of dynamic states, *Geophys. Res. Lett.*, *29*(9), 1352, doi:10.1029/2001GL013946, 2002.

Zwickl, R. D., et al., Plasma properties of driver gas following interplanetary shocks observed by ISEE-3, in *Solar Wind Five*, edited by M. Neugebauer, *NASA Conf. Publ., CP-2280*, 711, 1983.

S. K. Antiochos, E. O. Hulburt Center for Space Research, Naval Research Laboratory, Washington, DC 20375, USA. (antiochos@nrl.navy.mil)

L. A. Fisk, B. J. Lynch, and T. H. Zurbuchen, Department of Atmospheric, Oceanic, and Space Sciences, University of Michigan, Ann Arbor, MI 48109, USA. (lafisk@umich.edu; lynchb@engin.umich.edu; thomasz@umich.edu)